Monthly Notices of the ROYAL ASTRONOMICAL SOCIETY

MNRAS **475,** 492–507 (2018) doi:10.1093/mnras/stx3184
Advance Access publication 2017 December 9

ALMACAL – III. A combined ALMA and MUSE survey for neutral, molecular, and ionized gas in an H I-absorption-selected system

A. Klitsch,[1,2★] C. Péroux,[3] M. A. Zwaan,[1] I. Smail,[2] I. Oteo,[1] A. D. Biggs,[1] G. Popping[1,4] and A. M. Swinbank[2]

[1]*European Southern Observatory, Karl-Schwarzschild-Str. 2, D-85748 Garching Near Munich, Germany*
[2]*Centre for Extragalactic Astronomy, Department of Physics, Durham University, South Road, Durham DH1 3LE, UK*
[3]*Aix Marseille Univ., CNRS, LAM, (Laboratoire d'Astrophysique de Marseille), UMR 7326, F-13388 Marseille, France*
[4]*Max-Planck-Institut für Astronomie, Königstuhl 17, D-69117 Heidelberg, Germany*

Accepted 2017 November 27. Received 2017 November 24; in original form 2017 August 14

ABSTRACT

Studying the flow of baryons into and out of galaxies is an important part of understanding the evolution of galaxies over time. We present a detailed case study of the environment around an intervening Ly α absorption line system at $z_{\rm abs} = 0.633$, seen towards the quasar J0423−0130 ($z_{\rm QSO} = 0.915$). We detect with ALMA the ^{12}CO(2–1), ^{12}CO(3–2), and 1.2 mm continuum emission from a galaxy at the redshift of the Ly α absorber at a projected distance of 135 kpc. From the ALMA detections, we infer interstellar medium conditions similar to those in low-redshift luminous infrared galaxies. Director's Discretionary Time (DDT) Multi-Unit Spectroscopic Explorer (MUSE) integral field unit observations reveal the optical counterpart of the ^{12}CO emission line source and three additional emission line galaxies at the absorber redshift, which together form a galaxy group. The ^{12}CO emission line detections originate from the most massive galaxy in this group. While we cannot exclude that we miss a fainter host, we reach a dust-uncorrected star formation rate (SFR) limit of $>0.3\,{\rm M}_{\odot}{\rm yr}^{-1}$ within 100 kpc from the sightline to the background quasar. We measure the dust-corrected SFR (ranging from 3 to 50 $\rm M_{\odot}\ yr^{-1}$), the morpho-kinematics and the metallicities of the four group galaxies to understand the relation between the group and the neutral gas probed in absorption. We find that the Ly α absorber traces either an outflow from the most massive galaxy or intragroup gas. This case study illustrates the power of combining ALMA and MUSE to obtain a census of the cool baryons in a bounded structure at intermediate redshift.

Key words: ISM: molecules – galaxies: evolution – galaxies: formation – intergalactic medium – galaxies: ISM – quasars: absorption lines.

1 INTRODUCTION

A key part of understanding the evolution of galaxies is to determine how gas is accreted onto galaxies and how it is exchanged with their surroundings via outflows. Since ultimately the respective evolutions of gas, stars, and metals are connected through the stellar life cycle, gas flows have an immediate impact on the history of star formation (SF) and the chemical enrichment. Inflows of pristine gas might dilute the metal content of galaxies and certainly fuel their SF, whereas outflows take away the metals, chemically enriching the circumgalactic medium (CGM). High column density gas lying along a quasar line of sight is an ideal tool to study the CGM. These gas clouds characterized by Ly α or metal absorption profiles can probe not only a static CGM, but also flows of gas through the halo. To obtain a full picture of the CGM and its interplay with galaxies, it is important to study the location, kinematics, and metallicity of both the absorbing gas and the nearby galaxy.

Using integral field spectroscopy (IFS) it is possible to efficiently identify galaxies at the redshift of absorbers as well as determine their star formation rate (SFR), kinematics, and metallicity (e.g. Bouché et al. 2007; Péroux et al. 2011; Jorgenson & Wolfe 2014; Péroux et al. 2017). Interestingly, recent studies have shown that the identification of the Ly α absorber host galaxy is not always unique. In some cases, the absorber can be linked to one galaxy, but in other cases, it is associated with intragroup gas (Whiting, Webster & Francis 2006; Kacprzak, Murphy & Churchill 2010; Gauthier 2013; Bielby et al. 2017; Fumagalli et al. 2017; Péroux et al. 2017; Rahmani et al. 2018).

Recent studies have shown that the CGM extends to at least 100 kpc for isolated galaxies (Prochaska et al. 2017) and 140 kpc in groups of galaxies (Bordoloi et al. 2011). These distances convert

★ E-mail: aklitsch@eso.org

to a radial angular extent of ∼20 arcsec at intermediate redshifts of $z = 0.5$ requiring a large field-of-view integral field unit (IFU) such as Multi-Unit Spectroscopic Explorer (MUSE) to cover the full potential extent of the CGM.

Large surveys aiming to understand the connection between absorption line systems and their host galaxies either use galaxy–quasar pairs searching for absorption from the known galaxy in the quasar spectrum (e.g. Tumlinson et al. 2013) or target known absorbers and search for the associated galaxies using IFS (e.g. Schroetter et al. 2016; Bielby et al. 2017; Fumagalli et al. 2017; Péroux et al. 2017; Rahmani et al. 2018). Outflows are ubiquitously observed at all redshifts (e.g. Rupke, Veilleux & Sanders 2005; Veilleux, Cecil & Bland-Hawthorn 2005; Tremonti, Moustakas & Diamond-Stanic 2007; Weiner et al. 2009) while direct observations of inflows are less commonly found (e.g. Martin et al. 2012; Bouché et al. 2013), possibly because they are more difficult to observe.

A completely new perspective is opened by studying the molecular gas of the Ly α absorber host galaxy traced by ^{12}CO emission lines. Recently, Neeleman et al. (2016) reported the first detection of ^{12}CO(1–0) emission from such a host galaxy at $z = 0.101$. Moreover, the combination of ^{12}CO emission line detections with IFS, potentially allows us to get a complete census of the stars and the cool gas in such systems. This is the next important step towards a better understanding of such systems and therefore the flow of baryons through galaxies.

In our new (sub-)millimetre survey ALMACAL, we detect for the first time multiple ^{12}CO transitions from a galaxy first identified as an intervening absorber at $z_{\rm abs} = 0.633$ towards the quasar J0423−0130 ($z_{\rm QSO} = 0.915$). We have obtained additional MUSE observations revealing a group of four galaxies at the absorber redshift, where one of these is coincident with the ^{12}CO emission seen in the ALMA observations. The immediate aim of this study is to identify the origin of the absorption seen towards the quasar. In a broader perspective, this system serves us as a reference system to demonstrate the need for a multiwavelength study of intervening absorbers and their environment.

This paper is organized as follows. In Section 2, we describe our data set from the ALMA archive, the new MUSE observations, the ancillary archival data, and previous work. We describe the source detections and measurements from the ALMA and MUSE observations, the broad-band photometry based on archival data, and the analysis of the measurements in Section 3. In Section 4, we discuss possible scenarios explaining the absorption. A summary and the conclusions are given in Section 5. We present additionally morpho-kinematic modelling and the fitting of the absorption lines in the quasar spectrum in the Appendix. Throughout the paper, we adopt an $H_0 = 70\,{\rm km\,s^{-1}\,Mpc^{-1}}$, $\Omega_{\rm M} = 0.3$, and $\Omega_\Lambda = 0.7$ cosmology.

2 OBSERVATIONS AND DATA REDUCTION

The aim of this work is to identify and characterize galaxies connected to the intervening quasar absorber with a particular focus on the molecular gas content of the host galaxies. To do this, we use ALMACAL, a novel wide and deep (sub-)millimetre survey utilizing calibrator observations from the ALMA archive (Oteo et al. 2016).

From our parent sample, we have identified a particular absorber at $z = 0.633$ towards the quasar J0423−0130 ($04^{\rm h}23^{\rm m}15\overset{\rm s}{.}8$ $-01^{\rm d}20^{\rm m}33^{\rm s}$, $z = 0.915$). The absorber is a Lyman Limit System with an H I column density of $\log(N({\rm H\,I})/\,{\rm atoms\,cm^{-2}}) = 18.54^{+0.07}_{-0.10}$. We choose this source for our pilot study, because we detect two ^{12}CO emission lines in our ALMACAL data. We have obtained MUSE follow-up observations of the field. We show that combining these two data sets with other ancillary data yields a more complete picture of such systems.

Table 1. Summary of the used ALMACAL observations of J0423−0130.

Project code	Date	Scan Intent	Band	^{12}CO Trans.	$t_{\rm exp}$ (s)
2015.1.00920.S	09.01.2016	B	4	2−1	604.8
2015.1.00262.S	22.08.2016	B	4	2−1	728.5
2012.1.00350.S	04.12.2013	B	6	3−2	302.4
2013.1.00403.S	13.06.2014	B	6	3−2	302.4
2013.1.00111.S	05.07.2015	B	6	–	302.4
2013.1.01175.S	19.07.2015	B	6	–	605.8
2013.1.01175.S	19.07.2015	F	6	–	302.4
2013.1.01225.S	05.08.2015	B	6	–	302.4
2012.1.00146.S	28.05.2015	F	6	–	151.2
2015.1.00350.S	27.10.2015	B	6	–	302.4
2013.1.00198.S	06.06.2015	B	6	–	302.4
2013.1.01172.S	30.06.2014	B	6	–	483.8
2013.1.00815.S	28.06.2014	F	6	–	151.2
2013.1.00815.S	16.06.2014	B	6	–	604.8
2013.1.00710.S	12.12.2014	F	6	–	151.2
2015.1.00920.S	01.01.2016	B	6	–	302.4
2016.1.00724.S	27.12.2016	F	6	–	151.2
2016.1.00683.S	29.11.2016	F	6	–	151.2
2016.1.00627.S	03.12.2016	F	6	–	151.2
2016.1.00627.S	01.12.2016	F	6	–	302.4
2016.1.01453.S	22.11.2016	F	6	–	151.2
2016.1.01262.S	30.11.2016	F	6	–	151.2
2015.1.00296.S	22.06.2016	F	6	–	151.2

Note. Scan intent B denotes the bandpass calibrator, and F denotes the flux calibrator.

2.1 ALMACAL

The data used in this work are taken from the ALMACAL survey, a wide and deep survey utilizing the ALMA calibrator archive. The retrieval and calibration of the ALMA calibrator data are described in detail by Oteo et al. (2016).

Up until 2017 July 1, the quasar J0423−0130 was observed four times at frequencies corresponding to possible ^{12}CO emission lines at the absorber redshift. Two observations are available in Band 4 covering the frequency of the redshifted ^{12}CO(2–1) emission line and two observations in Band 6 covering the frequency of the redshifted ^{12}CO(3–2) emission line. The details of these observations are given in Table 1. The total integration time is 1333 s in Band 4 and 605 s in Band 6 for the observations covering the ^{12}CO emission lines. Furthermore, we use all well-calibrated Band 6 observations that do not cover the ^{12}CO(3–2) emission line to search for continuum emission. The corresponding data sets are listed in Table 1.

We carry out the calibration and data reduction using the Common Astronomy Software Applications (CASA) software package version 4.7. We examine each individual data set used for the emission line search first in the *uv* plane to apply further interactive flagging if necessary. We reduce the spectral resolution to a maximum of 15.625 kHz. This results in a velocity resolution of $33\,{\rm km\,s^{-1}}$ (and $66\,{\rm km\,s^{-1}}$ after Hanning smoothing) for the Band 4 observations and a velocity resolution of $22\,{\rm km\,s^{-1}}$ (and $44\,{\rm km\,s^{-1}}$ after Hanning smoothing) for the Band 6 observations. The spectral resolution ensures that an emission line with a width of $\gtrsim 300\,{\rm km\,s^{-1}}$ is covered by at least 5 and 7 channels in the respective bands. Before the imaging, we concatenate the two data sets in each band.

Table 2. Summary of the final J0423−0130 ALMA data cube properties.

Band	Freq (GHz)	med. Ang. Res. (arcsec)	rms (mJy beam^{-1})	Δv (km s^{-1})	PB FWHM (arcsec)
4	141.166	0.43	0.28	66	48
6	211.742	0.70	0.37	44	27

For the image cubes and the continuum image, the imaging was done using the standard 'clean' algorithm. A 'robust' weighting scheme was applied, using a Briggs parameter of 0.5, which guarantees a nearly optimal sensitivity while still providing a high spatial resolution and a well-behaved synthesized beam. In Band 4, we have two observations with a spatial resolution of 1.84 and 0.39 arcsec, and therefore we use an outer taper of 0.5 arcsec to prevent too high a weighting of the higher resolution data. The final parameters of the image cubes are given in Table 2. The resulting mean rms noise level in Band 4 is measured to be ∼0.28 mJy beam^{-1} per 66 km s^{-1} and the median angular resolution of the final data cube is ∼0.43 arcsec. The rms noise level in the Band 6 image cube is ∼0.37 mJy beam^{-1} per 44 km s^{-1} and the median angular resolution of the final data cube is ∼0.70 arcsec. The rms noise level in the 1.2 mm continuum image is ∼96 mJy beam^{-1} km s^{-1} and the median angular resolution is ∼0.75 arcsec. We use a pixel size of 0.15 arcsec in the Band 4 image cube, 0.24 arcsec in the Band 6 image cube covering the ^{12}CO(3–2) emission line, and 0.15 arcsec in the Band 6 continuum image cube.

2.2 New MUSE observations

We obtain MUSE observations in the field of J0423−0130 through Director's Discretionary Time. Although the previously identified galaxies from our ALMACAL observations and another galaxy identified in the broad-band imaging by Rao et al. (2011) are located south of the quasar, we centre the field of view on the quasar in order to not exclude a priori the possibility to find a galaxy north of the quasar. The observations were carried out in service mode under programme ESO 298.A-5017 at the European Southern Observatory using MUSE at the Nasmyth focus of the 8.2-m Very Large Telescope UT4. Two 'Observing Blocks' (OBs) were taken on 2016 December 23 and 24. The field is rotated by 180 deg between these two OBs. The OBs are further divided into two sub-exposures, with an additional rotation of 90 deg and a sub-arcsec dithering pattern. The exposure time of each sub-exposure is 1405 s with a seeing of 0.55–0.7 arcsec resulting in a total exposure time of 5620 s. The spectral coverage is ∼4800–9300 Å. At the redshift of the absorber ($z_{\rm abs} = 0.633$), we therefore cover all emission lines between [O II] and [O III], but not H α.

We reduce the data with v1.6.1 of the ESO MUSE pipeline and use the Zurich Atmosphere Purge (ZAP) code for the sky subtraction (Soto et al. 2016). We use the master bias, master flat-field and arc lamp exposures taken closest in time to the science observations to correct the raw data cubes. This is done with the SCIBASIC recipe. We do the correction to a heliocentric reference system using the SCIPOST recipe. In this step, we do not perform a sky-removal since ZAP is best performing on non-sky-subtracted cubes. We check the wavelength solution using the position of the brightest sky lines and find it to be accurate to 10 km s^{-1}. The offset table is created for each cube by comparing the positions of point sources in the field using the recipe EXP_ALIGN. In the final step, the cubes are combined using the recipe EXP_COMBINE. The seeing of the final cube measured from the quasar and other point sources is 0.71 arcsec at 7000 Å. To ensure a precise astrometry, we match the position of the quasar with its high-precision position known from Very Long Baseline Array (Lanyi et al. 2010).

We remove the sky emission lines using the ZAP code (Soto et al. 2016). To determine regions with pure sky emission a mask is created from the reconstructed white-light image. In this step, we set the flux levels accordingly to include bright objects in the mask. ZAP isolates the emission lines caused by sky emission using a principle component analysis and removes them from the data cube.

The quasar in this field is highly variable at optical wavelengths and we do not cover any other standard star with our field, so we estimate the flux error to be ±10 per cent based on our previous experience (Péroux et al. 2017; Rahmani et al. 2018).

2.3 Ancillary data

The target studied in this paper is the intervening metal-line absorber initially detected by Wills et al. (1980) as an Fe II and Mg II absorber at $z_{\rm abs} = 0.6320$ towards the quasar QSO J0423−0130 ($z_{\rm QSO} = 0.915$).

2.3.1 Early observations

This system was observed by several authors using narrow-band [O II] filters (Yanny, York & Williams 1990; Yanny & York 1992) and broad-band imaging (Churchill et al. 1996; Rao et al. 2011) to determine the galaxy associated with the intervening absorber. In total, six systems were reported with an impact parameter $\lesssim$200 kpc. However, no consensus was reached on what is causing the absorption. The coordinates of these galaxies are listed in Table 3.

2.3.2 Quasar spectroscopy

The strong Fe II and Mg II absorber was reobserved by Churchill et al. (1996) as part of a programme to study the spatial and velocity distribution of absorbing systems with known galaxy counterparts. The authors obtained a high-resolution spectrum of J0423−0130 in 1995 January using the HIRES echelle spectrometer (Vogt et al. 1994) on the Keck 10-m telescope. The spectral resolution is 6.6 km s^{-1}.

The absorber towards J0423−0130 was also part of an Mg–Fe II absorber sample, which was followed up by Rao, Turnshek & Nestor (2006) using the *Hubble Space Telescope (HST)* Space Telescope Imaging Spectrograph in Cycle 9 (PID 8569). The H I column density was determined to be $\log(N({\rm H\,I})/{\rm atoms\,cm^{-2}}) = 18.54^{+0.07}_{-0.10}$.

2.3.3 Imaging of the field of J0423−0130

Churchill et al. (1996) obtained broad-band imaging for the field of J0423−0130 and reported a galaxy associated with the absorber at an impact parameter of 14.7 kpc.

Table 3. Summary of all previously detected galaxies connected to the absorber towards J0423−0130.

ID	RA (J2000)	Dec. (J2000)	θ (kpc)	Previous Detection	Ref.	Detected in this Work
1	n.a.	n.a.	14.7	broad-band	Churchill et al. (1996)	No
2	04 23 15.58	−01 20 34.6	24.7	broad-band	Rao et al. (2011)	No
3	04 23 16.18	−01 20 46.9	102	[O II]	Yanny & York (1992), Rao et al. (2011)	Yes – J0423A
4	04 23 16.07	−01 20 52.1	133	[O II]	Yanny & York (1992)	Yes – J0423B
5	04 23 15.54	−01 20 54.0	146	[O II]	Yanny & York (1992)	Yes – J0423C
6	04 23 15.30	−01 21 03.7	216	[O II]	Yanny & York (1992)	Yes – J0423D

Note. For galaxy 1, Churchill, Steidel & Vogt (1996) only report the impact parameter, but not the coordinates. Yanny & York (1992) do not give the coordinates of the detected galaxies. Therefore, we match the galaxies with our observations and quote the coordinates based on this.

Furthermore, Rao et al. (2011) observed this field using the MDM Observatory 2.4-m Hiltner telescope. They analysed a 30 arcsec × 30 arcsec wide region of their images corresponding to a field of view of 205 kpc × 205 kpc at the absorber redshift. The images were taken in the *B*, *R*, *I*, *J*, *H*, and *K* bands. The point spread function (PSF) of the quasar was only subtracted in the optical bands. Rao et al. (2011) performed a stellar population synthesis modelling for the five sources they detected within a 100 kpc radius around the quasar. It was found that only one galaxy has a photometric redshift of $z = 0.637 \pm 0.031$ consistent with the absorber ($z_{\rm abs} = 0.6331$). The impact parameter of this galaxy is 14.5 arcsec or 99.6 kpc. Furthermore, it was reported that another source might be at an impact parameter of 3.6 arcsec, which would translate to 25 kpc at the absorber redshift. However, it was only visible in the infrared data and the spatial resolution prevented the isolation of the object from the quasar in these frames. Therefore, Rao et al. (2011) could not perform stellar population synthesis modelling for this source. The coordinates of the detected galaxies are given in Table 3. In the analysis, we use the broad-band images to obtain broad-band photometry of the MUSE-detected galaxies.

3 ANALYSIS

3.1 ALMA source detection and flux measurement

We aim to detect ^{12}CO emission from galaxies connected to the Lyman Limit System (LLS) at $z = 0.633$. Thus, we search for emission lines in the ALMA Band 4 and Band 6 image cubes using the Source Finding Application (SoFiA)[1] (Serra et al. 2015) that incorporates a number of different source detection algorithms to find emission lines in radio data cubes. We use the 'Smooth + Clip Finder', which uses an algorithm developed by Serra et al. (2012). It smooths the data in both spatial and spectral direction using a number of different 3D smoothing kernels. A search of emission lines is performed on each smoothed cube by detecting spaxels above a user-defined threshold. The complete discussion of the relative strengths and weaknesses of all possible source finding strategies is presented by Popping et al. (2012). We chose the 'Smooth + Clip Finder' since it offers the highest completeness and reliability for finding sources on a variety of scales. This is appropriate in our case since we do not know a priori whether our sources are spatially resolved. We use 12 smoothing kernels between 0.7 and 4.2 arcsec in the spatial dimension and between 66 and 990 km s^{-1} for the Band 4 data cube and 44 and 660 km s^{-1} for the Band 6 data cube in the spectral dimension. The detection threshold is 4σ for both data cubes. We require the detection to be within a range of ±2000 kms^{-1} relative to the absorber redshift, because we are targeting ^{12}CO emission at the absorber redshift. We run the source finder on the non-primary beam corrected cubes to ensure a constant noise level throughout the cube.

Using the detection method described above, we find ^{12}CO(2–1) and ^{12}CO(3–2) emission at the same position in the Band 4 and Band 6 cubes. We find no other emission lines which are detected in only one of the two data cubes. The emission lines are shown as contours in Fig. 1. The source is named J0423B throughout the paper. To our knowledge, this is the first time that multiple ^{12}CO transitions have been observed from one galaxy associated with a Ly α absorber. This allows us to investigate the properties of the interstellar medium in this galaxy.

We determine the size of the emission by fitting a two-dimensional Gaussian function to the integrated intensity maps. Here, we report the FWHM along the major axis deconvolved with the beam. The size of the ^{12}CO(2–1) emission is 1.3 ± 0.2 arcsec, the ^{12}CO(3–2) emission and the 1.2 mm continuum emission are not resolved.

Before extracting the spectra, we perform a primary beam correction on the image cube using IMPBCOR to account for the primary beam response function. We note that the primary beam correction at the position of our detected ^{12}CO lines in Band 6 is large because the ^{12}CO detection lies at 19.4 arcsec from the centre of the field, and the Band 6 primary beam width is only 13.5 arcsec. We determine the redshift of the ^{12}CO emission lines from the mean of the two frequencies at which the flux reached 50 per cent of the maximum flux density. The emission line spectra are shown in Fig. 2.

The flux is measured by integrating the spectra over two times the FWHM indicated by the yellow shaded region shown in Fig. 2. We have subtracted the continuum from the image cube using the task IMCONTSUB with a linear fit to the spectrum. We determine the width of the line profiles from the 50 per cent level of the maximum flux density. The observed line flux densities are converted to line luminosities using the following equation (Solomon, Downes & Radford 1992):

$$L'_{\rm line} = 3.25 \times 10^7 \times S_{\rm line}\Delta v \frac{D_{\rm L}^2}{(1+z)^3 f_{\rm obs}^2}\ {\rm K\,km\,s^{-1}\,pc^2}, \quad (1)$$

where $S_{\rm line}\Delta v$ is the observed velocity integrated line flux density in Jy km s^{-1}, $D_{\rm L}$ is the luminosity distance to the galaxy in Mpc, and $f_{\rm obs}$ is the observed line frequency in GHz. A summary of the emission line properties is given in Table 4. We estimate the error of the integrated line flux to be 5 per cent based on the expected accuracy of the flux calibration. The FWHM of the ^{12}CO emission lines is within the observed range for star-forming dusty galaxies at $z < 0.35$ (Villanueva et al. 2017). The projected impact parameter between the ^{12}CO detection and the quasar sightline is 133 kpc and

[1] https://github.com/SoFiA-Admin/SoFiA

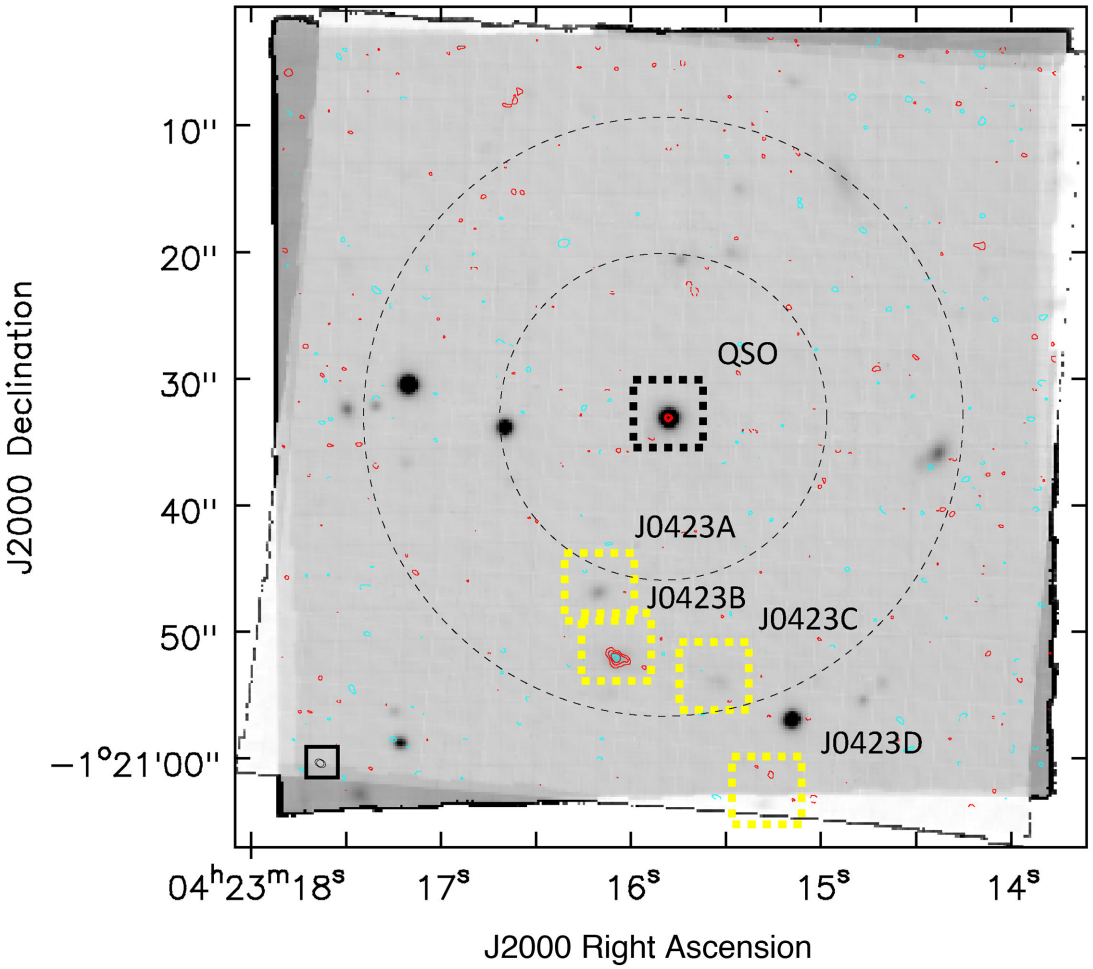

Figure 1. Overview of the detected sources in the field of J0423−0130. The reconstructed white-light image from our MUSE observations is shown in grey-scales, the red and cyan contours show the ^{12}CO(2–1) and ^{12}CO(3–2) emission, respectively. The contours show the -3σ, 3σ, 5σ, and 7σ levels in the respective maps, where negative contours are dashed. The galaxies identified to be at the absorber redshift based on out MUSE and ALMA observations are marked with the yellow boxes, the quasar is marked with the black box. The galaxies 1 and 2 in Table 3 are not detected in our observations and therefore not shown in the figure and not considered in the analysis presented here. The dashed large and small circles mark the ALMA half power beam width in Band 4 and Band 6, respectively. The small black circles in the bottom left corner show the synthesized beams of the ALMA Band 4 and Band 6 observations which have a comparable size. A zoom in on J0423B is shown in Fig. 3. The second OB of the MUSE observations was rotated by 5° with respect to the first OB due to a technical problem.

the position of the ^{12}CO detection is aligned with that of one of the galaxies detected in the MUSE cube. We discuss this in more detail in Section 3.2.

Furthermore, we combine all Band 6 observations from ALMACAL to search for continuum emission from the CO-detected galaxy. Hence, we can compare the total far-infrared luminosity based SFR with the SFR based on the dust-uncorrected [O II] emission line flux. We show in Fig. 3 (left) the Band 6 continuum map with the ^{12}CO (2–1) and ^{12}CO (3–2) emission line contours overplotted. We exclude any contamination from the ^{12}CO(3–2) emission line by excluding the data sets covering the relevant frequency. The total flux density at 1.2 mm is (0.8 ± 0.2) mJy and the peak intensity is (0.56 ± 0.09) mJy beam^{-1}.

Finally, we explore the possibility to observe molecular absorption lines towards the quasar in our Band 4 and Band 6 observations. The 3σ detection limit for the integrated optical depth is 0.01 and 0.003 km s^{-1} for ^{12}CO (2–1) and ^{12}CO (3–2), respectively. We note, however, that the velocity resolution is very coarse and might be not sufficient to detect absorption lines.

3.2 Muse source detection and flux measurement

We blindly search for line and continuum emission from galaxies in our MUSE cube. To this end, we search for emission line and continuum sources using the MUSELET source finding algorithm included in MPDAF.[2] MUSELET runs SEXTRACTOR (Bertin & Arnouts 1996) on each 1.25 Å wide slice of the cube to find any source of emission. We detect 50 emission line sources and continuum sources in the MUSE cube with this method. The galaxies at the absorber redshift ($z = 0.633$) are selected based on two criteria: (1) searching for emission line sources, and (2) by searching for the 4000 Å break at the rest frame of the absorber in all 50 spectra. We find four emission line sources at the absorber redshift, but we do not detect continuum sources at the absorber redshift. The full spectra of the four emission line galaxies are shown in Fig. 4. In Fig. 1, we mark the positions of these galaxies: J0423A, J0423B, J0423C, and J0423D.

[2] http://mpdaf.readthedocs.io/en/latest/

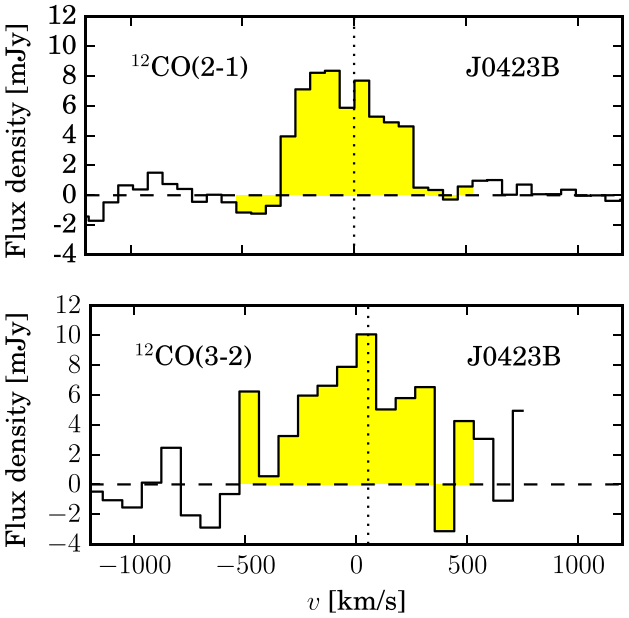

Figure 2. ^{12}CO(2–1) (top) and ^{12}CO(3–2) (bottom) emission lines observed in our ALMACAL data cubes centred in position on the quasar J0423−0130. The zero velocity corresponds to the redshift determined from the respective ^{12}CO emission line. The yellow region marks velocity range over which we integrate the total flux. The dotted lines show the position of the main absorption component at a redshift of 0.633 174. The peak in the ^{12}CO emission line redshift corresponds exactly with that of the Ly α absorption line, which signifies the clear association between the absorption system and the ^{12}CO gas. The spectra are binned to a resolution of 66 and 88 km s^{-1} for ^{12}CO(2–1) and ^{12}CO(3–2), respectively.

We determine the redshift of the galaxies by fitting a Gaussian to the detected emission lines. Since we detect multiple lines for all galaxies, we determine the redshift of each galaxy as the median redshift from the Gaussian fit to the detected lines. The respective redshifts and emission line fluxes are shown in Table 5. We do not detect [O III]4959 Å for any of our galaxies and therefore give only upper limits on the line flux. This is consistent with the expected line flux assuming a doublet flux ratio of 3 (Storey & Zeippen 2000). Furthermore, we detect H β in only two of the galaxies. The given upper limits are calculated from a maximum emission of 3σ and the FWHM measured from the sky emission lines corresponding to 3 Å. The line width of the detected lines determined from the Gaussian fitting is listed in Table 5.

In Fig. 3 (right), we show a comparison of the ALMA collapsed ^{12}CO emission line map and the MUSE pseudo-white-light image. It can be seen that the ^{12}CO gas is coincident with the optical position of galaxy J0423B. No emission from the other MUSE-detected galaxies is found in the ALMA cubes. Furthermore, comparing the FWHM of the [O III] lines and the ^{12}CO emission lines, we find that the molecular gas disc seems slightly more extended than the ionized gas.

3.3 Broad-band photometry and stellar mass

We estimate the stellar mass of the four galaxies, to infer the molecular gas mass ratio of J0423B and determine the total dynamical mass of the group. For this purpose, we use the broad-band imaging from Rao et al. (2011) to measure the broad-band photometry that we use as input for the spectral energy distribution (SED) fitting. The apparent magnitudes of the detected galaxies are determined using SEXTRACTOR and are listed in Table 5.

This broad-band photometry is used as input for the SED fitting with Le Phare[3] (Arnouts et al. 1999; Ilbert et al. 2006) to estimate the stellar masses of the galaxies. To perform the SED fitting, the algorithm compares the observed colours with the ones predicted from a set of template SEDs. We fix the redshift for the SED fitting to the spectroscopic redshift determined from our MUSE spectra described in Section 3.2. The template SEDs are convolved with standard B, R, I, J, H, and K filter functions and a χ^2 minimization is performed. We quote the stellar mass of the galaxies in Table 6. Comparing our stellar masses to the galaxy stellar mass function at redshift $0.4 < z < 0.6$ and $0.6 < z < 0.8$ for which Drory et al. (2009) report a $\log(M^\star)$ of $10^{10.91\,-\,10.95}$, we find that the CO-detected, most massive galaxy J0423B has a stellar mass of almost 2 M*, while the other galaxies J0423A, J0423C, and J0423D have stellar masses below $M^\star$.

3.4 Molecular gas mass

Until now the molecular gas content of galaxies associated with intervening Ly α absorbers has been determined only once (Neeleman et al. 2016). We combine the molecular gas mass with the stellar mass from the SED fitting to determine a census of the molecular gas and stars in galaxies associated with intervening absorbers. In the following, we determine the molecular gas mass using the two ^{12}CO emission lines. We use the following conversion:

$$M_{\rm mol} = \alpha_{\rm CO} \times L'_{\rm CO(1-0)}, \quad (2)$$

where $L'_{\rm CO(1-0)}$ is the luminosity of the ^{12}CO(1–0) emission line and the conversion factor $\alpha_{\rm CO}$ depends on the temperature, density, metallicity, and column density of the interstellar medium.

To apply the above-mentioned conversion to the total molecular gas mass, we need to convert the ^{12}CO(2–1) line flux to the ^{12}CO(1–0) line flux using a suitable conversion factor. The ratio of $L'_{\rm CO(3-2)}/L'_{\rm CO(2-1)}$ is 0.63 ± 0.09 suggesting a ^{12}CO excitation ladder similar to that of a luminous infrared galaxy (LIRG; Papadopoulos et al. 2012a). We note that this value is also consistent with the expected ratio of 0.54 for Milky Way type galaxies (Carilli & Walter 2013). However, based on further evidence presented in Section 4.1 we believe that the LIRG-type conversion factor is more appropriate. Therefore, we adopt a conversion factor of $L'_{\rm CO(2-1)}/L'_{\rm CO(1-0)} = 0.9$, yielding an $L'_{\rm CO(1-0)}$ of $(2.1 \pm 0.1) \times 10^{10}$ K km s^{-1} pc^2. Furthermore, we use $\alpha_{\rm CO} = 0.6\,{\rm M}_\odot\,({\rm K\,km\,s^{-1}pc^2})^{-1}$, appropriate for LIRGs derived by Papadopoulos et al. (2012b) including a factor of 1.36 to account for the presence of helium. This yields a molecular gas mass of $M_{\rm mol} = (1.27 \pm 0.07) \times 10^{10}\,{\rm M}_\odot$. To indicate the uncertainty in the derived H_2 mass, we also apply a conversion factor of $\alpha_{\rm CO} = 4.3\,{\rm M}_\odot\,({\rm K\,km\,s^{-1}pc^2})^{-1}$ typical for Milky Way type galaxies and including a factor of 1.36 to account for the presence of helium (Bolatto, Wolfire & Leroy 2013). This yields a molecular gas mass $9 \times 10^{10}\,{\rm M}_\odot$ and so we adopt a molecular gas mass of $1-9 \times 10^{10}\,{\rm M}_\odot$.

We have also extracted spectra from our ALMA cubes at the positions of J0423A and J0423C, but we could not find any clear sign of emission. For these two galaxies, we calculate upper limits for $L'_{\rm CO(2-1)}$ based on the 3σ noise level and assuming a width of the

[3] http://www.cfht.hawaii.edu/~arnouts/lephare.html

Table 4. ALMA detection of the galaxy J0423B.

Line	z	S_{peak} (mJy)	S_{int} (Jy km s^{-1})	L'_{CO} ($\times 10^{-10}$ K km s^{-1} pc^2)	FWHM (km s^{-1})
^{12}CO(2–1)	0.63317	8.4 ± 0.7	3.6 ± 0.2	1.9 ± 0.1	590 ± 30
^{12}CO(3–2)	0.63335	10 ± 1	5.2 ± 0.3	1.2 ± 0.1	610 ± 40

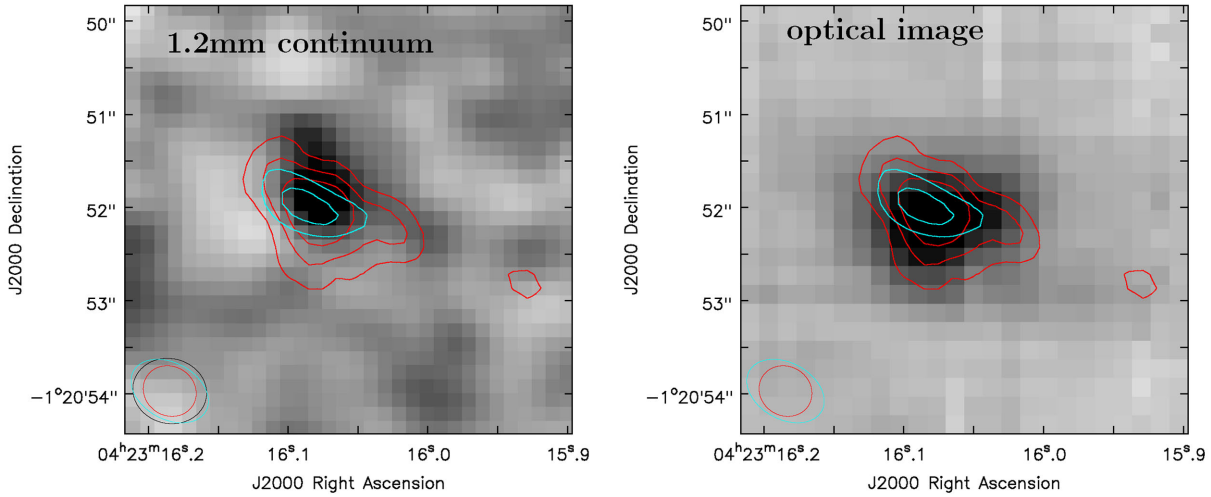

Figure 3. Zoom in on J0423B in Fig. 1. The 1.2 mm continuum emission is shown in grey-scales on the left and the MUSE reconstructed white-light image is shown in grey-scales on the right. In both panels, we show the ALMA ^{12}CO(2–1) in red contours, ALMA ^{12}CO (3–2) in cyan contours at 3σ, 5σ, and 7σ of the respective maps overlaid. The ellipses in the lower left corner show the beam size in the Band 4 and Band 6 observations, where the red ellipse corresponds to the beam in the ^{12}CO(2–1) line map, the cyan ellipse corresponds to the beam in the ^{12}CO(3–2) emission line map, and the black ellipse corresponds to the beam in the 1.2 mm continuum map. Negative contours are marked with dashed lines, but are not present in this close-up.

line of 500km s^{-1} based on the w_{50} measured from the ^{12}CO detections for J0423B. This yields an upper limit for the integrated flux of $S_{int} = 0.4$ Jy km s^{-1}, assuming that the flux is evenly distributed over the full width of the profile. Therefore, the upper limit on the line luminosity of $L'_{CO(2-1)}$ is 2×10^9 K km s^{-1} pc^2. We assume a Milky Way type $L'_{CO(2-1)}/L'_{CO(1-0)}$ emission line ratio of 0.5 (Carilli & Walter 2013) and a Milky Way type CO-to-H_2 conversion factor of $\alpha_{CO} = 4.3\,M_\odot\,(K\,km\,s^{-1}\,pc^2)^{-1}$ including a factor of 1.36 to account for the presence of helium (Bolatto et al. 2013). This yields an upper limit for the molecular gas mass of $M_{mol} < 1.7 \times 10^{10}$ $M_\odot$ for J0423A and J0423C.

3.5 Star formation rates

We determine the SFR of the CO-detected galaxy J0423B to test whether it is comparable with the identification of an LIRG based on the CO line flux ratios.

We estimate the SFR of J0423B based on the 1.2 mm flux. We use a set of template spectra for starburst galaxies from Polletta et al. (2007), which we scale to the observed 1.2 mm flux converted to the rest wavelength. The fitted spectrum is then integrated in the wavelength range from 8 to 1000 μm to obtain the total far-infrared luminosity L_{FIR}. This is converted to the SFR using the Kennicutt (1998) relation:

$$SFR_{FIR} = 4.5 \times 10^{-44} L_{FIR} \quad (3)$$

based on this, we estimate an SFR of (50 ± 10) $M_\odot$ yr^{-1}. We note, however, that the uncertainty in this calculation is high since we use the median SFR from a set of template spectra which we scale to the flux at 1.2 mm.

Furthermore, we derive the SFRs for the remaining three emission line galaxies based on the [O II] emission line using the relation given by Kennicutt (1998), which includes a dust correction:

$$SFR_{[O\,II]} = (1.4 \pm 0.4) \times 10^{-41} L([O\,II]) \times 10^{0.4A_{[O\,II]}}, \quad (4)$$

where $A_{[O\,II]}$ is the extinction of the [O II] emission line. We determine the dust correction based on the stellar mass dependent $A_{H\alpha}$ given by Garn & Best (2010) at $z \sim 0.1$, which is found to be valid up to $z \sim 1.5$ (Sobral et al. 2012). To convert the $A_{H\alpha}$ to $A_{[O\,II]}$ we use the prescription given by Calzetti (1997). The resulting dust-corrected SFRs are given in Table 6.

To test the identification of J0423B being an LIRG, we calculate the dust-uncorrected SFR based on the [O II] emission line for a comparison with the infrared-based SFR. We derive an SFR of 2.7 ± 0.3 $M_\odot$ yr^{-1} from the [O II] emission. This is 13–25 times lower than the SFR inferred from the far-infrared luminosity. This is in the lower envelope of the population of very luminous infrared galaxies studied by Poggianti & Wu (2000). This is a further piece of evidence that J0423B is an LIRG.

We determine the limiting SFR for our MUSE observations based on the detection limit of the [O II] line to infer the maximum SFR of potential galaxy candidates below our detection limit. The mean rms noise in the MUSE cube around the [O II] emission line is measured from the cube with a velocity width of 865 km s^{-1}. We perform a 3σ clipping on this cube and another 3σ clipping on the clipped cube to remove any contribution from actual emission. The mean rms noise is then determined from this emission-free cube. Furthermore, we assume that the minimum size of a galaxy is given by the seeing of 0.7 arcsec, which corresponds to 4.8 kpc at the absorber redshift and the FWHM of the line is at least 3 Å. The resulting [O II] flux would

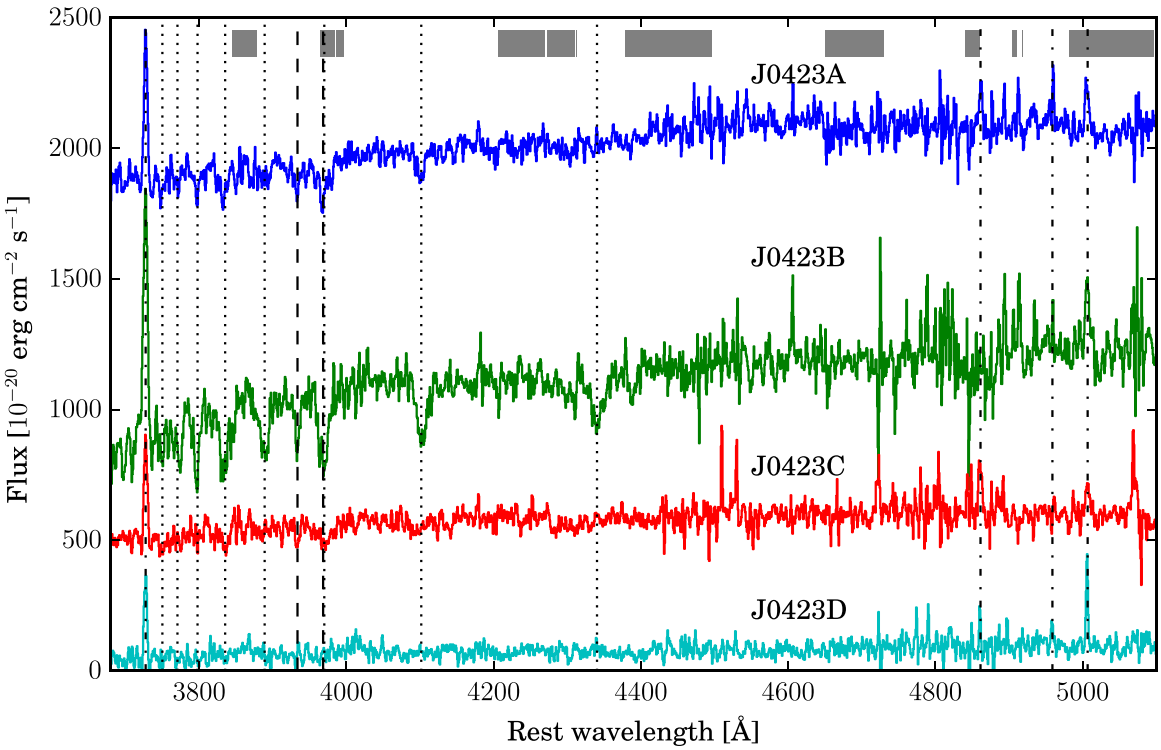

Figure 4. Rest-frame optical spectra of the four group members identified from our MUSE observation (offset by an arbitrary number for clarity). The spectra are shifted to rest wavelength using the redshift determined from the emission lines quoted in Table 5. The grey area marks the regions possibly contaminated by telluric absorption and emission. The strongest emission line in all spectra is [O II] at $\lambda = 3727$ Å. The dash–dotted line marks with increasing wavelength the [O II], H β, [O III]4959 Å, and [O III]5007 Å emission line. The dotted lines mark the Balmer absorption lines from H γ to H 12 with decreasing wavelength. The dashed lines mark the Ca H&K absorption lines. We note, that the features at the [O III]4959 Å and H β wavelength in J0423D as well as the narrow feature at the [O III]4959 Å wavelength in J0423A are marginal given the SNR of the spectrum.

Table 5. Observed properties of the galaxies from the MUSE observation and the broad-band imaging.

Name		J0423A	J0423B	J0423C	J0423D
RA (J2000)		04 23 16.18	04 23 16.07	04 23 15.54	04 23 15.30
Dec. (J2000)		−01 20 46.9	−01 20 52.1	−01 20 54.0	−01 21 03.7
θ (arcsec)		14.9	19.4	21.3	31.6
θ (kpc)		102	133	146	216
z		0.6332 ± 0.0005	0.6331 ± 0.0005	0.6338 ± 0.0003	0.6323 ± 0.0005
Line width	σ([O II])	170 ± 10	220 ± 10	170 ± 10	140 ± 10
	FWHM([O II])	400 ± 20	520 ± 30	390 ± 30	330 ± 30
	σ([H β])	120 ± 50	–	120 ± 40	–
	FWHM([H β])	290 ± 110	–	290 ± 90	–
	σ([O III]5007 Å)	150 ± 20	170 ± 30	160 ± 40	70 ± 20
	FWHM([O III]5007 Å)	360 ± 50	400 ± 70	380 ± 90	160 ± 40
Line fluxes					
(10^{-17} erg s^{-1} cm^{-2})	[O II]	5.3 ± 0.5	11.0 ± 1.1	3.6 ± 0.4	3.0 ± 0.3
	H β	1.7 ± 0.2	<0.9	1.7 ± 0.2	<2
	[O III] 4959	<0.9	<1	<0.6	<1
	[O III] 5007	2.1 ± 0.2	2.9 ± 0.3	1.3 ± 0.1	2.2 ± 0.2
B (mag)		23.8 ± 0.4	25.2 ± 0.5	24.6 ± 0.3	<25.82
R (mag)		22.10 ± 0.18	21.68 ± 0.18	22.72 ± 0.15	23.75 ± 0.17
I (mag)		21.0 ± 0.3	20.0 ± 0.2	21.8 ± 0.2	<25.15
J (mag)		20.43 ± 0.12	19.64 ± 0.09	20.90 ± 0.13	21.67 ± 0.11
H (mag)		19.83 ± 0.19	18.91 ± 0.12	20.3 ± 0.2	20.90 ± 0.19
K (mag)		19.87 ± 0.13	18.78 ± 0.08	20.34 ± 0.15	20.80 ± 0.11

Note. θ is the impact parameter given here in arcsec and kpc.

Table 6. Summary of the physical properties of the galaxies at the absorber redshift based on our MUSE data and the SED fitting.

Name	z	SFR ($M_\odot$ yr^{-1})	$\log M_\star$ ($M_\odot$)	12 + log(O/H)
J0423A	0.63317 ± 0.00048	7.5 ± 0.6	10.4 ± 0.2	8.80 ± 0.10^a
J0423B	0.63312 ± 0.00048	50 ± 10	11.2 ± 0.1	9.1 ± 0.9^b
J0423C	0.63376 ± 0.00032	4.6 ± 0.5	10.3 ± 0.2	8.94 ± 0.06^a
J0423D	0.63229 ± 0.00048	3.2 ± 0.5	10.2 ± 0.2	9.0 ± 0.9^b

Note. The SFRs of J0423A, J0423C, and J0423D reported in this table are based on the [O II] emission line and are dust corrected. The SFR of J0423B is derived from $L_{\rm FIR}$.
[a]The metallicity is determined from the emission lines.
[b]The metallicity is derived from the mass–metallicity relation.

be 0.3×10^{-17} erg s^{-1} cm $^{-2}$. This converts into a 3σ limiting SFR of 0.2 $M_\odot$ yr^{-1}. Additionally, we determine the limiting SFR at the quasar position. Therefore, we extract a 2 arcsec × 2 arcsec wide cube at the position of the quasar with a width of 865 km s^{-1} centred on the expected [O II] emission line covering all the observed [O II] emission. The emission from the quasar is determined by a linear fit and removed from the data cube. The limiting SFR at the position of the quasar is calculated from the noise in the continuum-subtracted cube and assuming the same emission properties as described above. This yields a non-dust-corrected limiting SFR of 0.3 $M_\odot$ yr^{-1}.

4 DISCUSSION

4.1 The nature of the galaxy J0423B

Galaxy J0423B is detected in ^{12}CO(2–1) and in the ^{12}CO(3–2) as well as in our MUSE observations. Here, we collect all this information and discuss the nature of this galaxy. In Section 3.4, it is shown that the ratio of the ^{12}CO(2–1) and the ^{12}CO(3–2) emission line is consistent with J0423B being an LIRG. Furthermore, the SFR based on $L_{\rm FIR}$ reported in Section 3.5 is $50 \pm 10\,M_\odot$ yr^{-1}. We compare this to the SFR from the dust-uncorrected [O II] line flux, which is 13–25 times lower. This is in the lower envelope of the very luminous infrared galaxy population studied by Poggianti & Wu (2000). Combining these pieces of evidence, we conclude that J0423B is an LIRG.

4.2 Assessing the possibility of a misidentification

The fact that we only detect galaxies at large impact parameters from the quasar sightline raises the question whether an undetected galaxy hiding in the bright quasar light could be responsible for the absorption. Interestingly, Churchill et al. (1996) report a galaxy at an impact parameter of 2.1 arcsec or 14.6 kpc and Rao et al. (2011) report another galaxy at an impact parameter of 3.6 arcsec or 25 kpc. We do not detect either of these galaxies in our data. In addition, these objects are not seen in quasar PSF-subtracted archival HST/NICMOS images (PID 7451). We determine the non-dust-corrected limiting SFR of 0.2 $M_\odot$ yr^{-1} over the full field of view and 0.3 $M_\odot$ yr^{-1} in a 2 arcsec × 2 arcsec wide field centred on the position of the quasar. We take this as the upper limit on the SFR of an undetected galaxy within the quasar PSF.

We compare the H I column density of the absorber and the impact parameter of the most massive group member with the column density – impact parameters observed for Lyman-alpha Absorbers (DLAs; Zwaan et al. 2005; Péroux et al. 2011) and sub-DLAs and LLS from the COS Halos survey (Prochaska et al. 2017) in Fig. 5. Assuming that J0423B can be uniquely associated with the Ly α absorption line, we see it is in the upper envelope of the relation between impact parameter and column density, but not atypical compared to other identified galaxy-absorption line pairs from the literature. This lessens the immediate need for another galaxy at a smaller impact parameter.

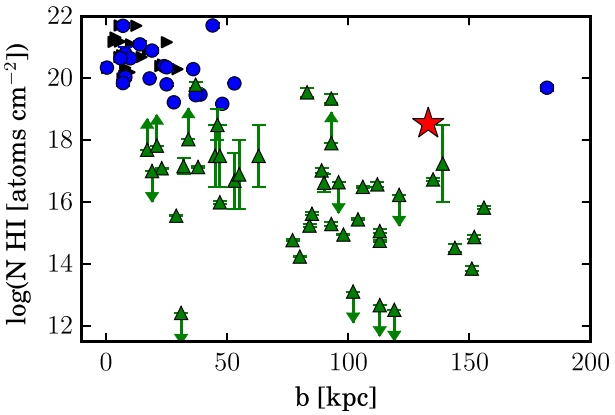

Figure 5. Column density of the intervening absorber as a function of impact parameter from J0423B (red star), DLAs from Zwaan et al. (2005, black triangles) and Péroux et al. (2011, blue circles), and sub-DLAs and LLS from the COS haloes survey (Prochaska et al. 2017, green triangles).

4.3 The nature of the absorbing gas

Here, we discuss the possibility that the absorbing gas is tracing an outflow or intragroup medium.

We consider whether the gas seen in absorption could be related to an outflow from one of the identified galaxies. In this galaxy group, an outflow is most likely starburst-driven and would therefore originate from J0423B. This is further supported by the morpho-kinematic properties of the galaxies studied in Appendix A. If we assume that the outflow of gas from galaxies is most efficient along the minor axis theoretically predicted by Kereš et al. (2009) and Stewart et al. (2011) and empirically motivated by recent studies (e.g. Bordoloi et al. 2011; Bouché et al. 2012; Schroetter et al. 2015), the best candidate having an outflow that could be probed by the absorption is J0423B. Furthermore, we assume a constant typical velocity of a galactic wind in a star-forming galaxy of 300 km s^{-1} (Veilleux et al. 2005). This yields a travel time of ∼430 Myr from J0423B to the position where we see the absorption. Recently, first attempts in theoretical modelling were made to understand how a cool outflow can be produced (Richings & Faucher-Giguere 2017).

Another explanation for the gas seen in absorption could be that it is tracing the intragroup medium. The MUSE observations revealed

four galaxies at the absorber redshift, which is an overdensity compared to the total redshift range. We expect, based on the [O II] luminosity function given by Ly et al. (2007), 0.05 galaxies above the limiting SFR within the MUSE field of view in a redshift range covered by the galaxy group. Therefore, we finally consider whether the gas seen in absorption against the background quasar is probing the CGM of the group of galaxies that we identify to be close in redshift space and in projected separation. We compare the alignment of the galaxies and the absorber in velocity space. In Fig. 6, we show the position of the absorber, the ^{12}CO detections from the ALMA observations, and the ionized gas detected with MUSE in velocity space with respect to the absorber redshift. We find that all galaxies align well with the absorber, where J0423C is redshifted by 200 km s^{-1} and J0423D is blueshifted by -250 km s^{-1} with respect to the absorber systemic velocity. This could indicate that the quasar absorption line probes the intragroup gas rather than the CGM of a single galaxy. Intervening absorbers are often found to trace intragroup gas at low redshift (Whiting et al. 2006; Kacprzak et al. 2010; Gauthier 2013; Bielby et al. 2017; Fumagalli et al. 2017; Péroux et al. 2017; Rahmani et al. 2018). In these cases, the velocity width of the absorption ranges from less than 100 km s^{-1} to more than 600 km s^{-1}. At this stage, we cannot distinguish intragroup gas from CGM based on this property.

The spatial extent of the CGM in group galaxies is reported to be more than 140 kpc and the intragroup gas can be even more extended (Bordoloi et al. 2011).

As an illustration, we compute an estimate of the dynamical mass of the group and the radius of the zero-velocity surface. To calculate the dynamical mass, we use the 'projected mass estimator' (Heisler, Tremaine & Bahcall 1985) defined by

$$M_{\rm PM} = \frac{32/\pi}{\mathrm{G}(N_{\rm m} - 1.5)} \sum_i v_i^2 r_i, \tag{5}$$

where G is the gravitational constant, $N_{\rm m}$ is the number of observed group members, v_i is the velocity of the group member i with respect to the group mean velocity, and r_i is the projected distance of the group member i from the group centre. Here, we define the most massive galaxy as the group centre since we cannot be sure that all group members are observed. This yields a dynamical mass of the group of $10^{12.9}\,\mathrm{M}_\odot$. Furthermore, we compute the radius of the zero-velocity surface, R_0, defined as the surface beyond which galaxies participate in the Hubble expansion (Sandage 1986). It is derived as follows:

$$R_0 = \left(\frac{8\,GT^2}{\pi^2} M_{\rm dyn}\right)^{1/3}, \tag{6}$$

where T is the age of the group. We assume that the age of the group is 7.5 Gyr, which is the age of the universe at the redshift of the group. This yields a radius of the zero-velocity surface of 1.2 Mpc. The gas that is probed by the Ly α absorption is well within this radius.

Furthermore, it is well known from nearby interacting groups that the group galaxies can be embedded in a large-scale atomic gas reservoir (Yun et al. 1994).

5 SUMMARY AND CONCLUSION

In this case study of an LLS at $z = 0.633$, we show the power of combining observations of the cool ionized gas with MUSE and ALMA observations of the ^{12}CO emission lines tracing the molecular gas in galaxies connected with a Ly α absorber. We measure two rotational transitions of the ^{12}CO line in emission, corresponding to

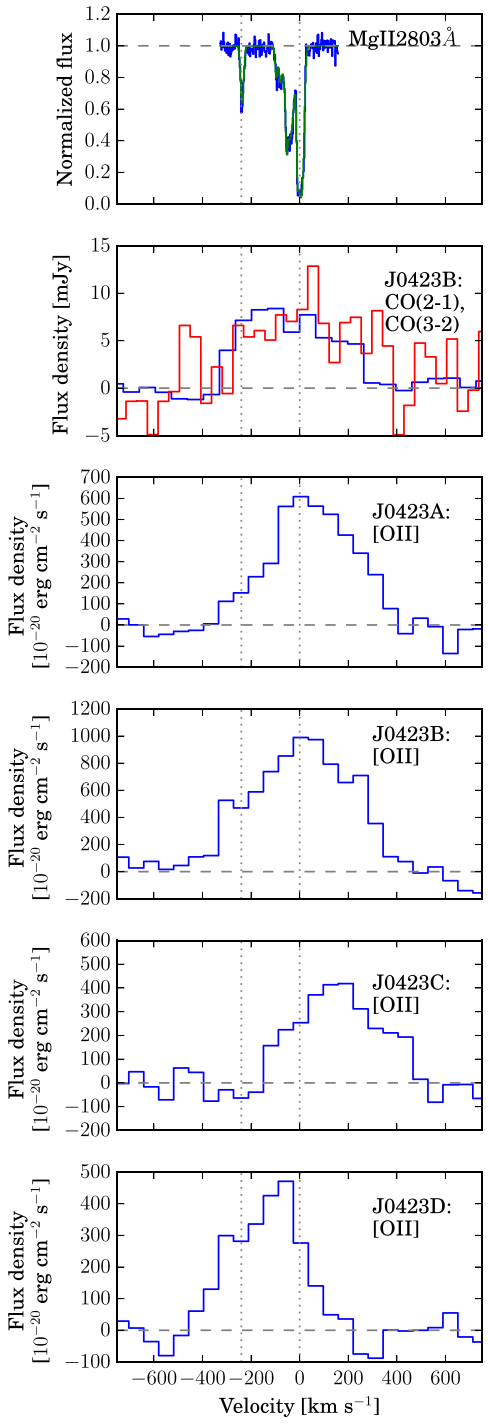

Figure 6. Comparison of all detected systems from top to bottom: Mg II absorption in the quasar spectrum from the HIRES spectrum, ^{12}CO(2–1) (blue) and ^{12}CO(3–2) (red) from J0423B from ALMACAL, the continuum-subtracted [O II] emission line spectra from J0423A, J0423B, J0423C, and J0423D all plotted relative to the absorber redshift. We stress that the width of the ^{12}CO and [O II] emission lines cannot be directly compared in this plot since the [O II] emission line doublet is not resolved in the MUSE observations.

a galaxy at the same redshift as the Ly α absorption line. This allows us to determine the molecular gas mass, as well as to put constraints on the ISM properties of this galaxy. We can efficiently identify star-forming galaxies at the absorber redshift using additional optical IFU observations. With these observations, we can probe the cool ionized gas in the galaxies and study their morpho-kinematics. In combination with the observations of the neutral gas probed in absorption, the observations of the cool ionized and molecular gas offer a complete census of the cool gas, which is needed to gain a better understanding of what types of galaxies are probed by Ly α absorbers.

In the particular system presented in this study, we find a group of massive galaxies with masses of $M_\star = 10^{10.3–11.2}\,M_\odot$ connected to an LLS with $\log(N(\mathrm{H\,I})/\mathrm{atoms\,cm^{-2}}) = 18.54^{+0.07}_{-0.10}$ at a redshift of $z = 0.633$. The impact parameter between the quasar sightline and the closest galaxy is 102 and 133 kpc for the most massive galaxy. No other galaxy is detected closer to the quasar down to a dust-uncorrected limiting SFR of $0.2\,M_\odot\,\mathrm{yr^{-1}}$ in the field and $0.3\,M_\odot\,\mathrm{yr^{-1}}$ at the quasar position. For the three lower mass galaxies, we find a dust-corrected SFR of $3\,M_\odot\,\mathrm{yr^{-1}} < \mathrm{SFR} < 7.5\,M_\odot\,\mathrm{yr^{-1}}$ and for the most massive galaxy we find an SFR based on the total far-infrared luminosity of $(50 \pm 10)\,M_\odot\,\mathrm{yr^{-1}}$.

The most massive galaxy is also detected in our ALMA ^{12}CO (2–1) and ^{12}CO(3–2) observations, from which we derive a molecular gas mass of $M_{H2} = 1–9 \times 10^{10}\,M_\odot$. We infer that this galaxy is likely to be an LIRG based on the emission line ratios as well as the ratio of the far-infrared-based SFR and the dust-uncorrected SFR based on the [O II] emission line flux. This is the first time that multiple ^{12}CO transitions are observed from one galaxy connected to a Ly α absorber. For the other galaxies in the field, we determine an upper limit of $M_{H2} < 17 \times 10^9\,M_\odot$.

We are able to model the morpho-kinematics of the three closest galaxies. As presented in Appendix A, all three galaxies have velocity fields consistent with a rotating disc. Moreover, we construct a line-of-sight velocity map from the ^{12}CO(2–1) emission line for J0423B. It is found that the velocity field from the cool ionized gas and the molecular gas are comparable.

We explore different explanations for the neutral gas probed in absorption.

(i) Another galaxy could be closer to the line of sight towards the quasar, which is not seen in our observations. The limiting dust-uncorrected SFR in our MUSE data cubes is $0.2\,M_\odot\,\mathrm{yr^{-1}}$ in the field and $0.3\,M_\odot\,\mathrm{yr^{-1}}$ at the position of the quasar. At this low SFR, the galaxy is unlikely to have an outflow and therefore it must be close to the quasar line of sight and the absorption is actually probing the ISM of this galaxy. We note that we cannot rule out this possibility completely, but we emphasize that our MUSE observations reach a higher completeness compared to previous studies using broad-band imaging.

(ii) The neutral gas could be tracing an outflow from the most massive galaxy J0423B since the quasar line of sight is aligned with the minor axis of the galaxy. We estimate, that for a constant outflow speed of $300\,\mathrm{km\,s^{-1}}$ it would take the gas 400 Myr to travel to the position of the absorber. However, the question remains how the gas can stay cool in the outflow or whether it can cool at larger distances. Furthermore, outflows of neutral gas are not yet observed at such large distances.

(iii) The impact parameter of 133 kpc for the most massive galaxy is comparable with the spatial extent of the intragroup gas quoted by Bordoloi et al. (2011). Moreover, recent studies frequently find intervening absorbers probing the intragroup gas. We argue that this is, apart from an undetected galaxy closer to the quasar line of sight, the most probable explanation for the gas traced by the absorption.

Finally, finding multiple galaxies at the absorber redshift adds further evidence to the findings by Whiting et al. (2006), Kacprzak et al. (2010), Gauthier (2013), Rahmani et al. (2018), Bielby et al. (2017), Fumagalli et al. (2017), and Péroux et al. (2017) suggesting that the classical picture of a one-to-one correlation between a Ly α absorber and the host galaxy is incomplete and needs to be revised.

ACKNOWLEDGEMENTS

We thank the anonymous referee for a constructive report. The authors thank Chris Churchill for kindly providing us with the reduced HIRES spectrum of the quasar and Sandhya Rao for kindly providing us with the broad-band images. We also thank Nicolas Bouché for his advice on the morpho-kinematic modelling using GALPAK^{3D}. The authors thank Hadi Rahmani for useful discussion about intragroup medium. We are grateful to the ESO staff at Paranal and in Garching for performing the MUSE observations in service mode. AK acknowledges support from the STFC grant ST/P000541/1 and Durham University. CP was supported by an ESO science visitor programme and the DFG cluster of excellence 'Origin and Structure of the Universe'. IRS acknowledges support from the ERC Advanced Grant DUSTYGAL (321334), a Royal Society/Wolfson Merit Award and STFC (ST/P000541/1). IO acknowledges support from the European Research Council in the form of the Advanced Investigator Programme, 321302, COSMICISM. This paper makes use of the following ALMA data:
ADS/JAO.ALMA#2015.1.00920.S,
ADS/JAO.ALMA#2015.1.00262.S,
ADS/JAO.ALMA#2012.1.00350.S,
ADS/JAO.ALMA#2013.1.00403.S.
ADS/JAO.ALMA#2013.1.00111.S,
ADS/JAO.ALMA#2013.1.01175.S,
ADS/JAO.ALMA#2013.1.01175.S,
ADS/JAO.ALMA#2013.1.01225.S,
ADS/JAO.ALMA#2012.1.00146.S,
ADS/JAO.ALMA#2015.1.00350.S,
ADS/JAO.ALMA#2013.1.00198.S,
ADS/JAO.ALMA#2013.1.01172.S,
ADS/JAO.ALMA#2013.1.00815.S,
ADS/JAO.ALMA#2013.1.00815.S,
ADS/JAO.ALMA#2013.1.00710.S,
ADS/JAO.ALMA#2015.1.00920.S,
ADS/JAO.ALMA#2016.1.00724.S,
ADS/JAO.ALMA#2016.1.00683.S,
ADS/JAO.ALMA#2016.1.00627.S,
ADS/JAO.ALMA#2016.1.00627.S,
ADS/JAO.ALMA#2016.1.01453.S,
ADS/JAO.ALMA#2016.1.01262.S,
ADS/JAO.ALMA#2015.1.00296.S,
ADS/JAO.ALMA#2013.1.01175.S,
and ADS/JAO.ALMA#2012.1.00650.S.

ALMA is a partnership of ESO (representing its member states), NSF (USA) and NINS (Japan), together with NRC (Canada), MOST and ASIAA (Taiwan), and KASI (Republic of Korea), in cooperation with the Republic of Chile. The Joint ALMA Observatory is operated by ESO, AUI/NRAO, and NAOJ. This work makes use of observations made with the NASA/ESA *Hubble Space Telescope*, or obtained from the data archive at the Space Telescope Institute (STScI), which is a collaboration between STScI/NASA, the Space

Telescope European Coordinating Facility (STECF/ESA) and the Canadian Astronomy Data Centre (CADC/NRC/CSA). This research made use of ASTROPY, a community-developed core PYTHON package for Astronomy (Astropy Collaboration 2013).

REFERENCES

Amorisco N. C., Bertin G., 2010, A&A, 519, A47
Arnouts S., Cristiani S., Moscardini L., Matarrese S., Lucchin F., Fontana A., Giallongo E., 1999, MNRAS, 310, 540
Asplund M., Grevesse N., Sauval A. J., Scott P., 2009, ARA&A, 47, 481
Astropy Collaboration, 2013, A&A, 558, A33
Belfiore F. et al., 2017, MNRAS, 469, 151
Bertin E., Arnouts S., 1996, A&AS, 117, 393
Bielby R., Crighton N. H. M., Fumagalli M., Morris S. L., Stott J. P., Tejos N., Cantalupo S., 2017, MNRAS, 468, 1373
Bolatto A. D., Wolfire M., Leroy A. K., 2013, ARA&A, 51, 207
Bordoloi R. et al., 2011, ApJ, 743, 10
Bouché N., Murphy M. T., Péroux C., Davies R., Eisenhauer F., Förster Schreiber N. M., Tacconi L., 2007, ApJ, 669, L5
Bouché N. et al., 2012, MNRAS, 419, 2
Bouché N., Murphy M. T., Kacprzak G. G., Péroux C., Contini T., Martin C. L., Dessauges-Zavadsky M., 2013, Science, 341, 50
Bouché N., Carfantan H., Schroetter I., Michel-Dansac L., Contini T., 2015, AJ, 150, 92
Calzetti D., 1997, AJ, 113, 162
Carilli C. L., Walter F., 2013, ARA&A, 51, 105
Christensen L., Møller P., Fynbo J. P. U., Zafar T., 2014, MNRAS, 445, 225
Churchill C. W., Steidel C. C., Vogt S. S., 1996, ApJ, 471, 164
Drory N. et al., 2009, ApJ, 707, 1595
Fumagalli M. et al., 2017, MNRAS, 471, 3686
Garn T., Best P. N., 2010, MNRAS, 409, 421
Gauthier J.-R., 2013, MNRAS, 432, 1444
Heisler J., Tremaine S., Bahcall J. N., 1985, ApJ, 298, 8
Ho I.-T., Kudritzki R.-P., Kewley L. J., Zahid H. J., Dopita M. A., Bresolin F., Rupke D. S. N., 2015, MNRAS, 448, 2030
Ilbert O. et al., 2006, A&A, 457, 841
Jorgenson R. A., Wolfe A. M., 2014, ApJ, 785, 16
Kacprzak G. G., Murphy M. T., Churchill C. W., 2010, MNRAS, 406, 445
Kennicutt R. C., Jr, 1998, ARA&A, 36, 189
Kereš D., Katz N., Fardal M., Davé R., Weinberg D. H., 2009, MNRAS, 395, 160
Kobulnicky H. A., Kewley L. J., 2004, ApJ, 617, 240
Lanyi G. E. et al., 2010, AJ, 139, 1695
Ly C. et al., 2007, ApJ, 657, 738
Maiolino R. et al., 2008, A&A, 488, 463
Martin C. L., Shapley A. E., Coil A. L., Kornei K. A., Bundy K., Weiner B. J., Noeske K. G., Schiminovich D., 2012, ApJ, 760, 127
Neeleman M. et al., 2016, ApJ, 820, L39
Oteo I., Zwaan M. A., Ivison R. J., Smail I., Biggs A. D., 2016, ApJ, 822, 36
Pagel B. E. J., Edmunds M. G., Blackwell D. E., Chun M. S., Smith G., 1979, MNRAS, 189, 95
Papadopoulos P. P., van der Werf P. P., Xilouris E. M., Isaak K. G., Gao Y., Mühle S., 2012a, MNRAS, 426, 2601
Papadopoulos P. P., van der Werf P., Xilouris E., Isaak K. G., Gao Y., 2012b, ApJ, 751, 10
Peng C. Y., Ho L. C., Impey C. D., Rix H.-W., 2002, AJ, 124, 266
Péroux C., Bouché N., Kulkarni V. P., York D. G., Vladilo G., 2011, MNRAS, 410, 2237
Péroux C., Kulkarni V. P., York D. G., 2014, MNRAS, 437, 3144
Péroux C. et al., 2017, MNRAS, 464, 2053
Poggianti B. M., Wu H., 2000, ApJ, 529, 157
Polletta M. et al., 2007, ApJ, 663, 81
Popping A., Jurek R., Westmeier T., Serra P., Flöer L., Meyer M., Koribalski B., 2012, PASA, 29, 318
Prochaska J. X. et al., 2017, ApJ, 837, 169
Rahmani H. et al., 2018, MNRAS, 474, 254
Rao S. M., Turnshek D. A., Nestor D. B., 2006, ApJ, 636, 610
Rao S. M., Belfort-Mihalyi M., Turnshek D. A., Monier E. M., Nestor D. B., Quider A., 2011, MNRAS, 416, 1215
Richings A. J., Faucher-Giguere C.-A., 2017, preprint (arXiv:1706.03784)
Rupke D. S., Veilleux S., Sanders D. B., 2005, ApJS, 160, 115
Sandage A., 1986, ApJ, 307, 1
Schroetter I., Bouché N., Péroux C., Murphy M. T., Contini T., Finley H., 2015, ApJ, 804, 83
Schroetter I. et al., 2016, ApJ, 833, 39
Serra P. et al., 2012, MNRAS, 422, 1835
Serra P. et al., 2015, MNRAS, 448, 1922
Sobral D., Best P. N., Matsuda Y., Smail I., Geach J. E., Cirasuolo M., 2012, MNRAS, 420, 1926
Solomon P. M., Downes D., Radford S. J. E., 1992, ApJ, 398, L29
Soto K. T., Lilly S. J., Bacon R., Richard J., Conseil S., 2016, MNRAS, 458, 3210
Stewart K. R., Kaufmann T., Bullock J. S., Barton E. J., Maller A. H., Diemand J., Wadsley J., 2011, ApJ, 738, 39
Storey P. J., Zeippen C. J., 2000, MNRAS, 312, 813
Tremonti C. A., Moustakas J., Diamond-Stanic A. M., 2007, ApJ, 663, L77
Tumlinson J. et al., 2013, ApJ, 777, 59
Veilleux S., Cecil G., Bland-Hawthorn J., 2005, ARA&A, 43, 769
Villanueva V. et al., 2017, MNRAS, 470, 3775
Vogt S. S. et al., 1994, in Crawford D. L., Craine E. R., eds, Proc. SPIE Conf. Ser. Vol. 2198, Instrumentation in Astronomy VIII. SPIE, Bellingham, p. 362
Weiner B. J. et al., 2009, ApJ, 692, 187
Whiting M. T., Webster R. L., Francis P. J., 2006, MNRAS, 368, 341
Wills B. J., Uomoto A. K., Wills D., Netzer H., 1980, ApJ, 237, 319
Yanny B., York D. G., 1992, ApJ, 391, 569
Yanny B., York D. G., Williams T. B., 1990, ApJ, 351, 377
Yun M. S., Ho P. T. P., Lo K. Y., 1994, Nature, 372, 530
Zahid H. J., Dima G. I., Kudritzki R.-P., Kewley L. J., Geller M. J., Hwang H. S., Silverman J. D., Kashino D., 2014, ApJ, 791, 130
Zwaan M. A., van der Hulst J. M., Briggs F. H., Verheijen M. A. W., Ryan-Weber E. V., 2005, MNRAS, 364, 1467

APPENDIX A: MORPHOLOGY AND KINEMATICS

To study the kinematics of the molecular gas, we create a line-of-sight velocity map using the CASA task IMMOMENTS including pixels where the ^{12}CO line emission is detected at 3σ above the noise in each velocity channel of the cube. The resulting map is shown in Fig. A1. The velocity field is sampled with only three resolution elements across the major axis, but given this limitation, the velocity field is consistent with that of a rotating disc.

To determine the morphology and kinematics of the four [O III]-detected galaxies in our MUSE cube, we perform a two-step analysis. First, we perform a Sérsic-fit of the [O III] pseudo-narrow-band image using GALFIT (Peng et al. 2002). Secondly, we use the GALPAK^{3D} algorithm (Bouché et al. 2015) to perform a 3D morpho-kinematic fit to the [O III] emission line cube. We use the Sérsic profile as input for the 3D morpho-kinematic fit. We infer from this fit whether the kinematics are compatible with that observed in a rotating disc and how the position angles of the galaxies are related to each other and how the quasar absorption is oriented with respect to the major and minor axes of the galaxies. However, given the data quality we will not be able to detect warps in the discs.

We determine the half-light radius, axis ratio, position angle (PA) and the Sérsic index from the [O III] pseudo-narrow-band image using GALFIT. This is a two-dimensional fitting algorithm extracting structural parameters from galaxy images. The algorithm models the light profile and is designed to fit multiple components. Here,

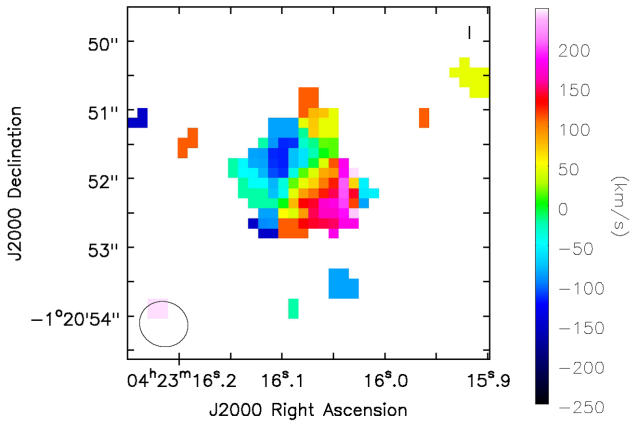

Figure A1. The intensity-weighted line-of-sight velocity field of the ^{12}CO(2–1) emission from the ALMA observations for J0423B. The velocity map is consistent with a rotating disc and the orientation is consistent with the model velocity field based on [O III] emission shown in Fig. A2.

we perform a single-component fit of the [O III] pseudo-narrow band image. The fitting results are shown in Table A1. We find that for J0423D the PA and Sérsic index are not very well constrained due to the low SNR of the detected line emission.

The GALPAK^{3D} algorithm is used to derive the kinematics of the galaxies based on the [O III] emission line. We do not use the [O II] emission line, because it is an unresolved doublet and we do not know the exact line ratio.

The GALPAK^{3D} algorithm directly compares a number of parametric models, created from a Markov Chain Monte Carlo (MCMC) algorithm and mapped in x, y, λ coordinate system, to the data. GALPAK^{3D} fits the model in three dimensions and offers even in poor seeing conditions a robust determination of the morpho-kinematics. It probes the posterior possibility density distribution via an MCMC chain of 15 000 runs and fits 10 parameters simultaneously (position (x, y, λ), flux, half-light radius, inclination, PA, turnover radius, maximum velocity, and intrinsic velocity dispersion).

The algorithm can only converge if the maximum SNR > 3 per pixel, which is not fulfilled for J0423D. Furthermore, the maximum velocity is overestimated if the ratio of galaxy half-light radius to seeing radius is smaller than about 1.5.

We use the half-light radius from the 2D fitting as a fixed input parameter for J0423B. For J0423A, it is necessary to fix the turnover radius to break the degeneracy with the maximum velocity. We set the turnover radius to 0.9 times the half-light radius based on the scaling relation found in local disc galaxies (Amorisco & Bertin 2010). Since all of the galaxies are found to be compact already from independent 2D profile fitting, we expect that the GALPAK^{3D} will overestimate the maximum velocity. The final fitting parameters are given in Table A1. We find that the velocity fields of the galaxies J0423A, J0423B, and J0423C are consistent with rotating discs. As can be seen in Table A1, the PAs from different objects are not aligned. Comparing the PA derived with GALPAK^{3D} with the PA from the 2D fitting with GALFIT, we find that they are comparable within the errors. We show the observed and model velocity fields from the MUSE observations in Fig. A2. It can be seen that in J0423B the velocity field of the ionized gas traced by the [O III] emission line and of the molecular gas traced by the ^{12}CO(2–1) emission line shown in Fig. A1 are consistent. Furthermore, we find that the angular extent of 1.4 ± 0.1 arcsec for the [O III] emission line matches the angular extent of 1.3 ± 0.2 arcsec found for the CO(2–1) emission line.

We explore the possibility that the absorption in the quasar spectrum is tracing the extended rotating gas disc of one of the two closest galaxies J0423A and J0423B. Therefore, we extrapolate the model velocity field derived above to the position of the absorber. The expected velocity is overplotted in the velocity space of the absorber on the Mg II2796 Å absorption line in the last panel of Fig. B1. It can be seen that the expected velocity from J0423A does not match the absorption profile. For J0423B on the other hand, we find that it agrees very well with one of the absorption components in the Mg II2796 Å absorption profile. Intriguingly, this galaxy is the one for which we measure a large cold gas content. We note, however, that projected separation between the quasar sightline and the gas-rich galaxy is 133 kpc, so the simple extrapolation of a rotating disc is a very naive assumption.

Table A1. Summary of the morphological parameters from 2D fitting and morpho-kinematic parameters from 3D fitting.

Name	$r_{1/2}^{\rm GALFIT}$ (kpc)	$r_{1/2}^{\rm GALPAK}$ (kpc)	PA$^{\rm GALFIT}$ (°)	PA$^{\rm GALPAK}$ (°)	$i^{\rm GALFIT}$ (°)	$i^{\rm GALPAK}$ (°)	Sérsic index	$v_{\rm max}^{\rm GALPAK}$ (km s^{-1})	$\sigma_0^{\rm GALPAK}$ (km s^{-1})
J0423A	1.5 ± 0.6	2.9 ± 0.3	106 ± 4	115 ± 4	33 ± 3	42 ± 6	3 ± 1	<410	11 ± 7
J0423B	2.77 ± 0.08	2.77[a]	90 ± 2	54 ± 24	40.5 ± 0.8	51 ± 17	1.04 ± 0.03	<170	84 ± 17
J0423C	1.54 ± 0.09	2.73 ± 0.03	67 ± 6	54 ± 21	47 ± 3	50 ± 16	0.71 ± 0.06	<191	87 ± 17
J0423D	0.5 ± 0.1		−90 ± 90		60 ± 30		0.3 ± 0.4		

Note. [a] is fixed based on the 2D fitting from GALFIT. We find that for J0423A, J0423B, and J0423C, the morphological parameters from independent 2D and 3D fitting are comparable.

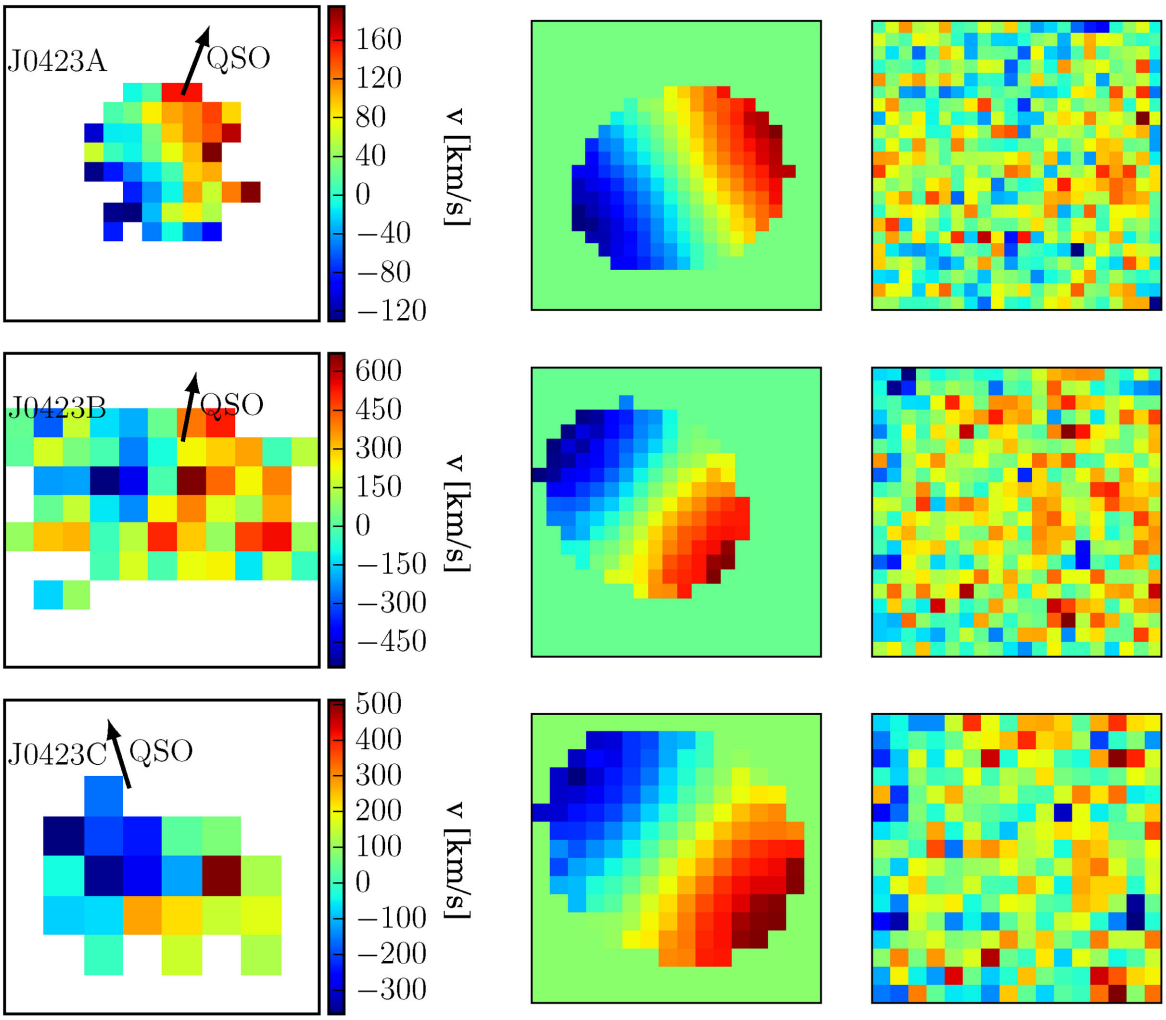

Figure A2. Results from the morpho-kinematic fitting to the [O III] emission detected with MUSE, including the observed velocity field (left), the model velocity field from GALPAK^{3D} fitting (middle) and the residual map (right) for J0423A (top), J0423B (middle), and J0423C (bottom). The arrow indicated the direction towards the quasar sightline. We find that all three galaxies have velocity fields consistent with rotating discs. We caution that the maximum velocity from the modelling is uncertain because all three galaxies are very compact (<3 kpc) and GALPAK^{3D} is known to overestimate the maximum velocity in the case of compact galaxies (Bouché et al. 2015). We also note that the observed velocity fields are spatially re-sampled for display purpose.

APPENDIX B: NEUTRAL GAS PROPERTIES

In this section, we use the quasar spectrum presented by Churchill et al. (1996) to fit the absorption lines, determine the minimum number of components needed to reproduce the absorption profile and determine their redshift. We will use these fits in Section C2 to derive a lower limit on the total metallicity of the absorbing neutral gas. We use the kinematic information and the metallicity of the absorber to infer the alignment with the galaxies in velocity space as well as the possibility of probing an extended galactic disc with the absorption.

We model the metal absorption lines in the quasar spectrum associated with the LLS with Voigt profiles using VPFIT[4] v.10.2. The VPFIT code is developed to fit multiple Voigt profiles to spectroscopic data by minimizing the χ^2. Here, we have performed a multicomponent fit assuming that for each absorption component all ions have the same redshift. We show the spectra and the Voigt profile fits in Fig. B1. It can be seen that the Mg II2803 Å and Mg II2796 Å absorption lines are saturated and more complex than the Fe II2600 Å, Fe II2382 Å, and Mg I2852 Å absorption lines. Therefore, we fit the two sets of absorption lines separately. We find that the absorption lines are well fitted using two components for the Fe II and Mg I lines. A separate fit is performed for the strong Mg II lines using six components. We summarize the corresponding fit parameters in Table B1.

[4] https://www.ast.cam.ac.uk/~rfc/vpfit.html

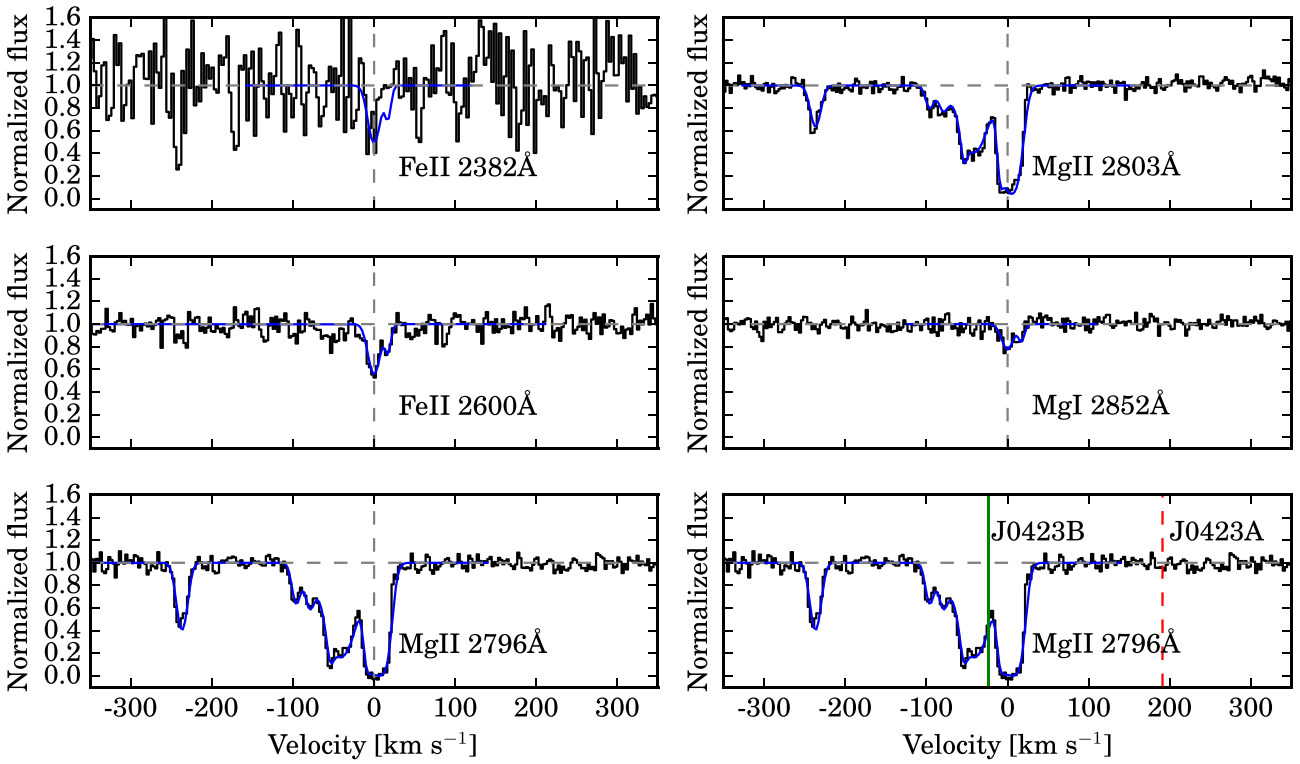

Figure B1. Fits to the Fe II2382 Å, Fe II2600 Å, Mg II2796 Å, Mg II2803 Å, and Mg I2852 Å absorption lines in the QSO spectrum. In the fitting using VPFIT we assumed two components for Fe II and Mg I and six components for the saturated Mg II. Velocity zero corresponds to the redshift of the main component from the joint fits of Fe II26007thinsp;Å, Fe II2382 Å, Mg I2852 Å. The last panel shows a comparison of the Mg II2796 Å absorption line profile with the expected absorption caused by an extended rotating disc of J0423A and J0423B at the position of the quasar sightline. We find that the absorption cannot be caused by an extended disc of J0423A, but the velocity extrapolated from the disc of J0423B matches the absorption profile. We note, however, that due to the large impact parameter of 133 kpc, the absorption is unlikely tracing the disc of J0423B.

Table B1. Fit parameters for the absorption line Voigt profile fitting using VPFIT.

Ion	No.	z	b	log N (atoms cm^{-2})
Fe II	1	0.633 174 ± 0.000 006	3.0 ± 2.4	12.21 ± 0.13
Fe II	2	0.633 080 ± 0.000 005	8.9 ± 1.4	12.80 ± 0.05
Mg I	1	0.633 174 ± 0.000 006	3.0 ± 2.4	11.04 ± 0.15
Mg I	2	0.633 080 ± 0.000 005	8.9 ± 1.4	11.50 ± 0.07
Mg II	1	0.631 791 ± 0.000 002	7.7 ± 0.5	12.49 ± 0.02
Mg II	2	0.632 558 ± 0.000 005	5.7 ± 1.3	12.09 ± 0.06
Mg II	3	0.632 648 ± 0.000 005	7.0 ± 1.8	12.16 ± 0.08
Mg II	4	0.632 788 ± 0.000 003	2.9 ± 1.4	12.36 ± 0.09
Mg II	5	0.632 855 ± 0.000 004	20.6 ± 0.9	13.17 ± 0.02
Mg II	6	0.633 108 ± 0.000 003	11.5 ± 0.4	13.49 ± 0.04

Notes. The top four rows above the dividing line show the parameters for the Voigt Profile fitting using only Fe II and Mg I. The bottom six lines below the dividing line show the fit parameters for the Voigt profile fit using only the Mg II absorption lines. No. denotes the number of the component that is simultaneously fit in multiple absorption lines.

APPENDIX C: METALLICITIES

We study the metallicity of the ionized gas in the galaxies and of the neutral gas traced by the absorption. Using this information, we can compare the metallicities observed at different positions with each other and infer from this the connection between the galaxies and the absorbing gas.

C1 H II metallicities

To determine the gas metallicities of the MUSE-detected galaxies from the emission lines, we use the R23 method as first introduced by Pagel et al. (1979), which is widely used to determine gas metallicities if the H β, [O II], and [O III] fluxes are known. It uses the log R_{23} parameter, which is defined as follows:

$$\log(R_{23}) = \log\left(\frac{F([O\,\text{II}]\lambda3727, 3729) + F([O\,\text{III}]\lambda4959, 5007)}{F(\text{H}\,\beta)}\right). \quad \text{(C1)}$$

We derive the metallicities according to the formalism described as the 'best' oxygen abundance determined by Kobulnicky & Kewley (2004). We use the O32 parameter ($f_{[\text{O III}]}/f_{[\text{O II}]}$) as a branch indicator (Maiolino et al. 2008), where O32 > 2 suggests the lower branch solution and O32 <1 suggests the upper branch solution. The four galaxies in this study have O32 values between 0.26 and 0.74 indicating that the upper branch solution is appropriate. The derived metallicities of our galaxies are listed in Table 5. Compared to the solar abundance of log(O/H) + 12 = 8.69 (Asplund et al. 2009), we find that galaxies J0423A and J0423C have metallicities of 0.11 and 0.25. However, since we are not applying a dust correction we could overestimate the metallicities.

Since we do not detect the H β emission line from J0423B and J0423D, we use the stellar mass–metallicity relation to determine the gas phase metallicity of these two galaxies. We use the relation

Table C1. Metallicity of the galaxies and expected metallicity based on extrapolation using a constant slope at the absorber position assuming an extended gas disc.

Name	$Z_{\rm mean}$	$Z_{\rm central}$	θ(kpc)	$Z_{\rm exp}/Z_{\odot}$
J0423A	0.1 ± 0.1	0.2 ± 0.1	102	-2 ± 1
J0423B	0.4 ± 0.9	0.5 ± 0.9	133	-3 ± 1
J0423C	0.25 ± 0.06	0.32 ± 0.06	146	-3 ± 2
J0423D	0.3 ± 0.9	0.3 ± 0.9	216	-5 ± 2

Note. $Z = 0$ is equal to the solar abundance.

given by Zahid et al. (2014), who fits the following function to a sample from DEEP2 at $z \simeq 0.8$:

$$12 + \log(\mathrm{O/H}) = \mathrm{Z}_0 + \log\left(1 - \exp\left(-\left[\frac{\mathrm{M}_\star}{\mathrm{M}_0}\right]^\gamma\right)\right), \qquad \text{(C2)}$$

where $Z_0 = 9.10$, $\log(M_0[\mathrm{M}_\odot]) = 9.80$, and $\gamma = 0.52$. This yields a metallicity of $12 + \log(\mathrm{O/H}) = 9.1 \pm 0.9$ and 9.0 ± 0.9 for J0423B and J0423D, respectively. The 1σ scatter in the DEEP2 data is quite large, and therefore the derived metallicity has a large error bar.

C2 Neutral gas metallicity

We use the combined fits of Fe II2600 Å and Fe II2382 Å and the H I column density derived by (Rao et al. 2006) to determine the metallicity of the absorbing gas without taking dust into account. We report a lower limit to reflect possible ionization correction. We find that $[\mathrm{Fe/H}] = \log(\mathrm{Fe/H})_{\rm abs} - \log(\mathrm{Fe/H})_\odot$ is higher than -1.16.

C3 Comparison

Large integral field surveys have shown that galaxies with $\log(M_\star) > 9.6$ have a uniform metallicity gradient within the disc of -0.026 dex kpc^{-1} (Ho et al. 2015). However, at distances beyond $2R_{\rm e}$ first pieces of evidence for a flattening of the metallicity gradients are found (Belfiore et al. 2017). For absorption line systems, a similar shallow negative metallicity gradient is observed out to 25 kpc (e.g. Christensen et al. 2014; Péroux, Kulkarni & York 2014; Rahmani et al. 2018). In the system presented in this work, the impact parameter is >100 kpc and therefore much larger than the ones probed in the aforementioned studies. We test whether we can connect the galaxies with the absorbing gas using a uniform metallicity gradient. We extrapolate the metallicity observed in the four galaxies to the position of the intervening absorber using a constant gradient from the literature. First, we derive the central metallicity of the galaxies from the total metallicity reported in Table 6 and using the solar abundance of log(O/H) + 12 = 8.69 (Asplund et al. 2009). To derive the central metallicity, we assume a linear distribution of the mean metallicity quoted in Table C1 over two $r_{1/2}$, where we use $r_{1/2}$ from the 3D fitting if available. We use the standard metallicity gradient determined within the disc quoted above. The same metallicity gradient is then used to extrapolate the derived central gas phase metallicity to the position of the absorber. The mean and central metallicity of the galaxies and the expected metallicity at the position of the absorber are given in Table C1. We find that the extrapolated metallicity is above a simple extrapolation of the metallicity gradient. This shows that the metallicity gradient cannot be extended to such large distances.

However, here we are comparing the metallicity of the ionized gas in the galaxy with the metallicity of neutral gas probed by the absorption. Furthermore, the standard deviation in the observed gradients is ± 0.010 dex kpc^{-1} in the study by Ho et al. (2015). The corresponding uncertainty in the extrapolation is shown in Table C1. Considering this and the additional caveat of using uniform gradients discussed above, we regard this calculation only as an indication.

This paper has been typeset from a TEX/LATEX file prepared by the author.